Numerical Analysis of 3D Unilateral Quasi-static Contact: Effect of Coating Thickness and Mechanical Properties

Andel Djamai[*]*, Hamid Zaidi*
Institut Pprime UPR3346-IUT, Université de Poitiers, Futuroscope, F-86960, Poitiers, FRANCE
[*]*hamid.zaidi@univ-poitiers.fr*

Djamel Bekhouche, Ali Bouchoucha
Laboratoire de Mécanique, Faculté des Sciences de la technologie, UFMC1, ALGERIE

ABSTRACT

In this study, a numerical model for unilateral quasi-static contact between a rigid sphere and an elastic coating has been developed. The contact problem was solved using a numerical procedure based on the FFT technique, considering various coatings with different thicknesses and mechanical properties, implemented through a Matlab code. The model calculates the contact surface deformation and pressure field through a double iteration process. The first iteration solves the contact problem for a given indenter penetration, while the second iteration refines this penetration by minimizing the difference between the fixed and calculated loads. To achieve this, influence coefficients are derived from the elasto-static equations using the Papkovich-Neuber potentials. The study discusses the influence of coating thickness and friction coefficient value on the tribological behavior of the coating. The results indicate that contact pressure increases (ranging from 1.9 to 2.5) as the coating becomes thicker or more rigid (0.02 mm to 0.2 mm). Additionally, the tribological behavior of the coated surface is affected by the coating's thickness, hardness, and friction coefficient value. Importantly, this model demonstrates versatility by being applicable to both smooth and rough surfaces.

Keywords: *Elastic Coating; Friction; Contact Pressure; Stress Field; Numerical Model*

ISSN 1823-5514, eISSN 2550-164X

https://doi.org/10.24191/jmeche.v21i3.27342

Received for review: 2022-11-21
Accepted for publication: 2023-08-01
Published: 2024-09-15

Introduction

It is well established in the industry that thin layer coatings of a few tens of micrometres considerably improve the tribological properties and increase the service life of mechanical components. To machine at high speed, manufacturers and research laboratories have optimized the choice of coating materials to withstand the contact temperature. However, machining or rubbing under high applied normal load requires optimization of the coating thickness. Indeed, the maximal Hertzian shear stress is localized in the contact sub-surface and its localization depth depends on the friction coefficient value and the mechanical properties of the coating/substrate. For the coating to play its protective role, numerical modelling of the contact is necessary to locate the shear stress in the coating under a given applied normal load.

For a solid contact sphere/plane without coating, the Hertzian theory [1] provides us with all the necessary equations. If N is the applied normal load, then the contact radius a_0, the indenter penetration δ, and the contact pressure p_0 are given by the following equations:

$$a_0 = \left(\frac{3NR}{4E^*}\right)^{1/3}, \delta = \frac{a_0^2}{R} = \left(\frac{9N^2}{16RE^{*2}}\right)^{1/3}, p_0 = \left(\frac{6NE^{*2}}{\pi^3 R^2}\right)^{1/3} \quad (1)$$

$$\frac{1}{E^*} = \frac{1-\nu_1^2}{E_1} + \frac{1-\nu_2^2}{E_2} \quad (2)$$

where R is the indenter radius and E^* is the equivalent Young's modulus of the two bodies in contact.

There are several numerical methods, such as the method of the finite differences, the finite elements, the integral method, the inverse method, the hybrid method, and the Frontiers' method to calculate the contact stress field [2]. The finite element method is often used to solve problems of contact. It makes it possible to study solids of arbitrary geometries and laws of various rheological behavior. However, the formulations used are complex and the implementation of this method is difficult.

The methods of solving the inverse problem are numerous and depend on the hypotheses established on the stress fields in the contact. If the normal problem is simple to solve, the tangential problem is more complicated. The three-dimensional contact is generally little treated because a fine discretization of the contact zone is necessarily important to obtain good precision, but it induces a very long computation time.

Conry and Seireg [3] presented a method applied to 2D contact while neglecting tangential efforts. Chiu and Hartnett [4] proposed an algorithm to solve normal 3D contact with a loop on the displacement of a solid body. This

method is impractical because it includes four embedded convergence loops. Nogi and Kato [5] presented a resolution method for a coated medium rough contact. The influence coefficients are expressed in the Fourier space where the resolution of the contact problem is also realized. This method has the advantage compared to a classical method, to decrease the computation times considerably thanks to the application of a convolution product in the Fourier space instead of a summation of the influence coefficients in real space. Kalker [6] develops a contact algorithm with three-dimensional friction for smooth surfaces.

O'Sullivan and King [7] presented a model based on a least squares iterative approach that determines the field of contact pressure between a sphere and a coating. Their results were validated by Peng and Bhushan [8], based on a variational principle minimizing the potential energy. Another model has been presented by Stepanov and Torskaya [9]. Plumet and Dubourg [10] introduced FFT into their model to solve the contact of a rigid ellipsoid on a coating. Wang et al. [11] and Yinhu et al. [12] presented a 3D contact model for studying the partial slip contact on 3D elastic layered half-space, using a numerical procedure based on the conjugate Gradient method and fast Fourier transform technique. In recent work, Wang et al. [13] developed a numerical approach for analyzing three-dimensional steady-state rolling contact including creep using a semi-analytical method. Another similar semi-analytical method has been designed by Manyo et al. [14] based on Kalker's theory coupled with Conjugate Gradient algorithms and FFT.

On the other hand, the modeling of viscoelastic 3D rolling contacts has been treated by many researchers [15]-[19]. In more recent work Wallace et al. [20] propose for the first time a method to solve the 3D contact problem with a viscoelastic multi-layered half-space. Bettayeb and Villechaise [21] used it for a thermoelastic resolution of a coated bearing. Another model is based on the inversion method of the influence matrix. Gupta and Walowit [22] made use of it to solve a 2D indentation of a cylinder. However, it does not guarantee numerical convergence when the number of contact points is important or when the surface profile is complex. Additionally, the effect of various parameters on the sliding contact response in pure sliding contact problems of functionally graded coating-substrate like the friction coefficient [23], indenter profile [24], and surface effects or frictional heat [25]-[29] have been widely investigated.

The article presents a numerical simulation that allows for obtaining the pressure field and induced displacements in the z-direction and calculating the total normal force, given the penetration of the supposed rigid sphere. Secondly, it lets us vary the penetration of the ball (sphere) until the acquisition of the desired normal force. The displacements of the contact surface are then obtained. What remains to calculate then, is the stress tensor in all points of the coating or in the substrate to which a double inverse FFT is applied, knowing of the pressure field.

The advantage or the strength of this modeling calculation, based on the displacement field optimization until obtaining the applied normal load on the contact, and to be able to calculate a smooth or rough surface. Additionally, the convergence of the method is relatively fast and guaranteed.

Contact Model

Deformation of the contact surface

The numerical model simulates the contact between a perfectly rigid spherical indenter and a coating of thickness h, Young's modulus E_1 and Poisson's ratio v_1 deposited on a half-space solid of Young's modulus E_2 and Poisson's ratio v_2 as indicated on Figure 1.

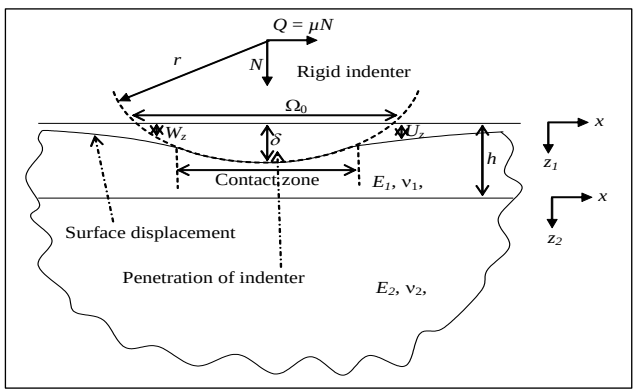

Figure 1: The contact model and notations in the *xz*-plane

The displacement W_z the following z-axis, represents that of the rigid sphere, between the sphere and the coating. This displacement is given according to the following geometrical relation:

$$W_z(x,y) = \sqrt{r^2 - (x^2 + y^2)} - (r - \delta) \tag{3}$$

where δ represents the penetration of the sphere. This model is supposed to be in the linear elastic range. The adhesion between surfaces in contact will be neglected, that is, all the pressures are positive or zero on the surface.

Boundary conditions

The boundary conditions on surface $z_1 = 0$ are given by:

$$\begin{aligned}\sigma_{zz}^{(1)}(x,y,0) &= -P(x,y,0),\\ \sigma_{xz}^{(1)}(x,y,0) &= \mu P(x,y,0),\\ \sigma_{yz}^{(1)}(x,y,0) &= 0\end{aligned} \tag{4}$$

There is a continuity of displacements and stresses at the interface between the coating and the substrate:

$$\begin{aligned}\sigma_{xz}^{(1)}(x,y,h) &= \sigma_{xz}^{(2)}(x,y,0), \qquad u_x^{(1)}(x,y,h) = u_x^{(2)}(x,y,0)\\ \sigma_{yz}^{(1)}(x,y,h) &= \sigma_{yz}^{(2)}(x,y,0), \qquad u_y^{(1)}(x,y,h) = u_y^{(2)}(x,y,0)\\ \sigma_{zz}^{(1)}(x,y,h) &= \sigma_{zz}^{(2)}(x,y,0), \qquad u_z^{(1)}(x,y,h) = u_z^{(2)}(x,y,0)\end{aligned} \tag{5}$$

The stress tensors and the displacements are zero at a very long distance from the loading point:

$$\sigma^{(2)}(x,y,\infty) = 0, \qquad u^{(2)}(x,y,\infty) = 0 \tag{6}$$

The suffixes (1) and (2), respectively refer to the coating and the substrate.

Construction of the influence matrix C

To calculate the displacement on each point of the coating surface, a mesh of this surface will be defined, as indicated in Figure 2. In space or real domain, the total surface is discretized by N_xN_y grids of the unit surface $\Delta_x\Delta_y$. In the frequency domain, grids of the size $(2\pi/N_x\Delta_x)(2\pi/N_y\Delta_y)$ are used for the meshing. The total surface to mesh is of the size $(2\pi/\Delta_x)(2\pi/\Delta_y)$. On each grid of meshing, the pressure is supposed constant.

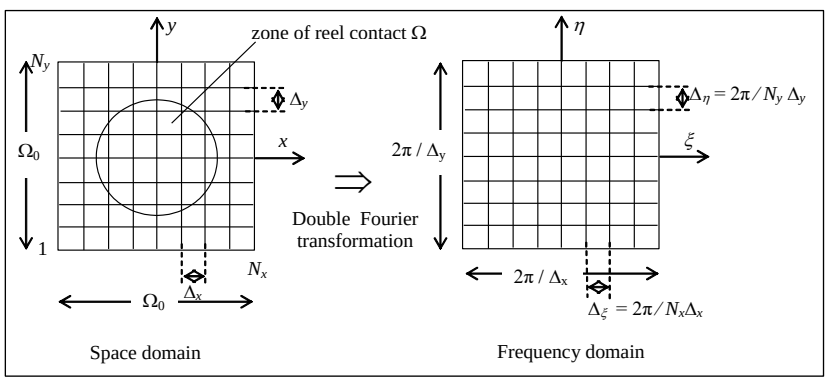

Figure 2: Discretization of the contact surface in space and frequency domain

The procedure used to calculate the influence matrix coefficients is presented in this paragraph. Being given a pressure field on all the surface points, the displacement at the point k (x_k, y_k, z_k) of the surface noted u_k is related to the coefficients of the influence matrix by the following relation:

$$u_k = \sum_{l=1}^{m} C_{kl} P_l \text{ or in matrix form: } \begin{pmatrix} u_1 \\ . \\ . \\ u_m \end{pmatrix} = \begin{pmatrix} C_{11} & . & . & C_{1m} \\ . & . & . & . \\ . & . & . & . \\ C_{m1} & . & . & C_{mm} \end{pmatrix} \begin{pmatrix} P_1 \\ . \\ . \\ P_m \end{pmatrix} \quad (7)$$

where m represents the total number of meshing points: $m = N_x N_y$ and C_{kl} refers to the displacement at the point k due only to a constant pressure P_l applied to the point $l(x_l, y_l, 0)$. For an isotropic material, this element of the influence matrix depends only on the geometrical distance of the two points k and l. It is given by the following expression:

$$C_{kl} = C(|x_l - x_k|, |y_l - y_k|, |z_l - z_k|) = C(|x_l - x_k|, |y_l - y_k|, 0) = C(x, y, 0) \quad (8)$$

The influence matrix coefficients are generated by using the potentials of Papkovitch-Neuber. These potentials φ and $\psi = (\psi_1, \psi_2, \psi_3)$ are harmonic functions that are dependent on x, y, and z. Malvern [30], showed that the four functions can be reduced to three by choosing $\psi_2 = 0$. The displacements and the stresses are given according to these potentials by:

$$\begin{aligned} 2Gu_i &= \phi_{,i} + x\psi_{1,i} + z\psi_{3,i} - (3-4\nu)\psi_i \\ \sigma_{ij} &= \phi_{,ij} - 2\nu(\psi_{1,1} + \psi_{3,3})\delta_{ij} - (1-2\nu)(\psi_{i,j} + \psi_{j,i}) + x\psi_{1,ij} + z\psi_{3,ij} \end{aligned} \quad (9)$$

where index i, and j being worth 1, 2, and 3 respectively refer to x, y, and z. δ_{ij} is the symbol of Kronecker. G is the ratio between the shear modulus of the coating G_1 and that of the substrate G_2.

A double Fourier transform is applied to the system of two Equations (9) to eliminate the derivative terms, and to transform the space potentials of Papkovitch-Neuber into frequency potentials, using the following equation:

$$\bar{C}(\xi_m, \eta_n) = TF(C(x, y)) = \sum_{i=1}^{N_x} \sum_{j=1}^{N_y} e^{-i(x_i \xi_m + y_j \eta_n)} C(x_i, y_j) \quad (10)$$

where $m = 1 \ldots N_x$, and $n = 1 \ldots N_y$, noting respectively ξ and η the variables associated with x, y in the frequency domain (Figure 2). In the same way, the double inverse Fourier transform was defined by:

$$C(x_i, y_j) = \overline{TF}(\bar{C}(\xi,\eta)) = \frac{1}{N_x N_y}\sum_{m=1}^{N_x}\sum_{n=1}^{N_y} e^{i(x_i\xi_m + y_j\eta_n)}\bar{C}(\xi_m,\eta_n) \quad (11)$$

with $i = 1\ldots N_x$ and $j = 1\ldots N_y$. However, it is much more judicious, when calculating a double inverse Fourier transform of a continuous function $f(\xi,\eta)$, to generate a finer mesh of this function in the frequency domain in order not to lose information on this function at the time of its sampling (by increasing the number of points only in the frequency domain). Equation (11) becomes then:

$$C(x_i, y_j) = \overline{TF}(\bar{C}(\xi,\eta)) = \frac{1}{N_\xi N_\eta}\sum_{m=1}^{N_\xi}\sum_{n=1}^{N_\eta} e^{i(x_i\xi_m + y_j\eta_n)}\bar{C}(\xi_m,\eta_n) \quad (12)$$

with $i = 1\ldots N_x$ and $j = 1\ldots N_y$, by taking $N_\xi > N_x$ and $N_\eta > N_y$. The Fourier transform of Papkovitch-Neuber potentials for the coating in the frequency domain is given by:

$$\bar{\phi}^{(1)} = A^{(1)}e^{-\alpha z_1} + \bar{A}^{(1)}e^{\alpha z_1}, \bar{\psi}_1^{(1)} = B^{(1)}e^{-\alpha z_1} + \bar{B}^{(1)}e^{\alpha z_1}, \bar{\psi}_3^{(1)} = C^{(1)}e^{-\alpha z_1} + \bar{C}^{(1)}e^{\alpha z_1} \quad (13)$$

In the substrate, these potentials are given by:

$$\bar{\varphi}^{(2)} = A^{(2)}e^{-\alpha z_2} + \bar{A}^{(2)}e^{\alpha z_2}, \bar{\psi}_1^{(2)} = B^{(2)}e^{-\alpha z_2} + \bar{B}^{(2)}e^{\alpha z_2}, \bar{\psi}_3^{(2)} = C^{(2)}e^{-\alpha z_2} + \bar{C}^{(2)}e^{\alpha z_2} \quad (14)$$

where $\alpha = \sqrt{\xi^2 + \eta^2}$ and $\bar{A}^{(2)} = \bar{B}^{(2)} = \bar{C}^{(2)} = 0$ because of the boundary conditions (6). By using the boundary conditions (4) and the conditions of continuity on the stress and displacements (5), a linear system of nine equations with nine unknowns was obtained $A^{(1)}, \bar{A}^{(1)}, B^{(1)}, \bar{B}^{(1)}, C^{(1)}, \bar{C}^{(1)}, A^{(2)}, B^{(2)}, C^{(2)}$ which can be solved analytically. By substituting expressions of the nine unknowns in the Fourier transform of the two Equations (9), the displacements and the stress expressed in the frequency domain were obtained. It is then enough to apply an inverse Fourier transform to find them in the spatial domain.

The influence coefficients can be thus expressed and are given in the frequency domain by:

$$\bar{C}(\xi_m,\eta_n) = -\left(\frac{1-\nu_1}{G_1}\right)\alpha R(1 + 4\alpha hke^{-2\alpha h} - \lambda ke^{-4\alpha h}) \quad (15)$$

where;

$$G_1 = \frac{E_1}{2(1+\nu_1)},\ G_2 = \frac{E_2}{2(1+\nu_2)}, \text{ and } G = \frac{G_1}{G_2}$$

$$\lambda = 1 - \frac{4(1-\nu_1)}{1+G(3-4\nu_2)}, k = \frac{G-1}{G+(3-4\nu_1)}, \text{ and}$$

$$R = -\left\{(1-(\lambda + k + 4k\alpha^2 h^2)e^{-2\alpha h} + \lambda k e^{-4\alpha h})\alpha^2\right\}^{-1}$$

Let us note that the size of the matrix $\bar{C}$ is $N_\xi N_\eta$ (by applying Equation (11) because $\bar{C}$ is continuous). On the other hand, the size of the matrix C is $(N_x N_y)$ $(N_x N_y)$ according to Equation (7) because Equation (8) is used to calculate all these terms.

Once the matrix C is calculated, the relation between the vector P and the displacement vector U_z becomes a bijective relation (for each displacement vector, there exists only one pressure vector and inversely).

Calculation of the pressure field and vertical displacement of the surface

The calculation procedure of the pressure field is divided into two parts:

a) in the first part, the penetration of the indenter was set, and the displacement vector and pressure field were then calculated.
b) in the second part, the penetration is related to the total applied normal force F resulting from the pressure field. The penetration is thus varied until a total force, F equal to the required force N is found.

The algorithm of the program is given in Figure 3. In this part, the procedure of calculation will be detailed:

After fixing the penetration, a computational field is created with sufficient size in the spatial field to encompass the complete real contact area, as shown in Figure 2 (for example a lateral square one and a half times the contact area estimated from the Hertz Equation (3), or take a square with R side). The initial displacement of our model is defined as U_0:

$$U_0 = \begin{cases} W_z \text{ in the contact zone } \Omega_0 \\ 0 \text{ outside} \end{cases} \tag{16}$$

Note: the value of U_0 outside Ω_0 is not known a priori. An artifice of calculation will be used by giving a null value outside the Ω_0 field.

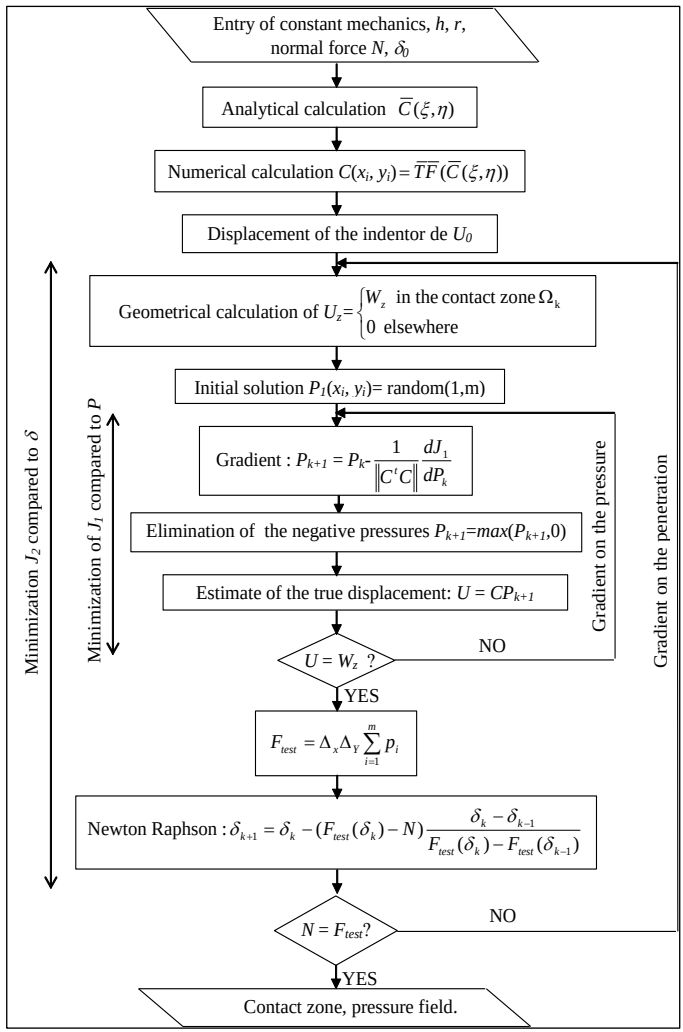

Figure 3: Program Algorithm

A vector of initial pressure, P_0 of size m, is generated on all our space fields defined by a random function. The problem thus consists of finding a pressure field solution of the U_z problem $U_z = CP$ (here $U_z = U_0$). This is equivalent to minimizing the criterion J defined by:

$$J_1 = \|U_z - CP\|^2 = (U_z\text{-}CP)t(U_z\text{-}CP) \qquad (17)$$

For that purpose, a gradient method is applied where the negative pressures corresponding to the pressures being located outside the contact zone Ω_0 are eliminated with every iteration. The displacement considered real, $U_k = C\ P_k$, is then recalculated by using the new positive or null pressures. The gradient is stopped as soon as the displacement U_k obtained is equal to the displacement W_z on the new contact zone. The final zone of contact corresponds then to the field where the pressure field is different from zero. This gradient is defined by:

$$P_{k+1} = P_k - \alpha \frac{dJ_1}{dP_k} = P_k + \alpha C \left(U_0 - CP_k\right) \tag{18}$$

When a Newtonian algorithm is considered, allowing convergence in a step in the vicinity of the optimal solution of the gradient, then α is given by:

$$\alpha = \left(\frac{d^2 J_1}{dP_k^2} \right)^{-1} = (C^t C)^{-1} \tag{19}$$

To cure the problem of inversion of large-sized matrices (dimension of C^tC is $(N_x\ N_y)\ (N_x\ N_y)$), a choice is made:

$$\alpha = \left\| C^t C \right\|^{-1} \tag{20}$$

the gradient becomes:

$$P_{k+1} = P_k + \frac{C}{\left\| C^t C \right\|} \left(U_0 - CP_k\right) \text{ et } P_{k+1} = max\ (P_{k+1},\ 0) \tag{21}$$

Once the Pressure field is determined for a fixed penetration δ_0, which corresponds to a normal force equal to $F_{test} = \Delta_x \Delta_Y \sum_{i=1}^{m} p_i$, but it does not remain more to be varied δ_0 (thus U_z) until obtaining $F_{test} = N$ by using a second gradient acting on the penetration, the criterion to be minimized is:

$$J_2 = \left| N - F_{test} \right|^2 \tag{22}$$

and the gradient is defined by:

$$\delta_{k+1} = \delta_k - \beta \frac{dJ_2}{d\delta_k} \tag{23}$$

Not having an explicit relation $F_{test} = f(\delta)$, the following algorithm is chosen:

$$\delta_{k+1} = \delta_k + \beta(N - F_{test}) \tag{24}$$

where $\Delta\delta = \beta(N-F_{test})$ corresponds to the quantity added or withdrawn from the penetration in each iteration. Let us note what $\Delta\delta$ could have been selected as being constant, however, it is more judicious to choose its increasing function of the difference between N and F_{test} to reduce the iteration count ($\Delta\delta$ large if $|N - F_{test}|$ large, and $\Delta\delta$ small if $|N - F_{test}|$ small). In our calculations, it is taken into account $\beta = 10^{-8}$ *m/N* allowing us to accelerate the algorithm to the maximum while ensuring its convergence.

In the calculations of this study, a condition was fixed to stop the calculation, which corresponds to a difference between F_{test} and N lower than 0.1 N. The displacement is then calculated thanks to Equation (8) using the obtained pressure field, by application of the two gradients.

Results and Discussion

Pressure and contact zone

The model described above is used to simulate a unilateral quasi-static contact between a rigid sphere and an elastic coating. The radius of the sphere is r = 0.2 mm, Young's modulus of the substrate is E_2 = 200 *GPa*, and that of the coating E_1 chosen for five cases is respectively 50, 100, 200, 400, and 800 *GPa*. The Poisson's ratios v_1 and v_2 are fixed at 0.3. The results are presented for three values of the thickness of coatings $h = r/10$, $h = r/5$, and $h = r$.

The contact pressure is normalized by the maximum pressure P_0 obtained in the center of the indenter in the case $E_1 = E_2$. The x- and y-coordinates are devised by radius a_0 of the contact zone for $E_1 = E_2$. The z-coordinate is dimensioned by the coating thickness, h.

Figures 4(a), 4(b), and 4(c) present the profiles of the pressures obtained respectively in the three cases where $h = r/10$, $h = r/5$, and $h = r$ for various values of E_1/E_2. Figure 4(c) represents, in the case $E_1 = E_2$, the profile of the pressure obtained by the solution of Hertz in the case of a half-space mass charged by the same spherical indenter. This pressure corresponds perfectly to the solution given by this model.

For the same thickness of the coating, the radius of the contact zone decreases with the increase of the ratio E_1/E_2 and increases when E_1/E_2

decreases. The maximum pressure in the center of the contact zone increases if E_1/E_2 increases and it acts inversely on the contrary case.

If the coating is stiffer than the substrate ($E_1>E_2$), the maximum pressure tends to increase if the coating thickness is increased. The distribution of pressure becomes more pointed. If the coating is softer than the substrate ($E_1<E_2$), the maximum pressure decreases when the coating thickness is decreased. The distribution of the pressure then becomes larger and flatter and flatter (Figure 4(a)). Figure 5 represents the evolution of the ratio (a/a_0) according to the ratio (h/r) for various ratios of (E_1/E_2).

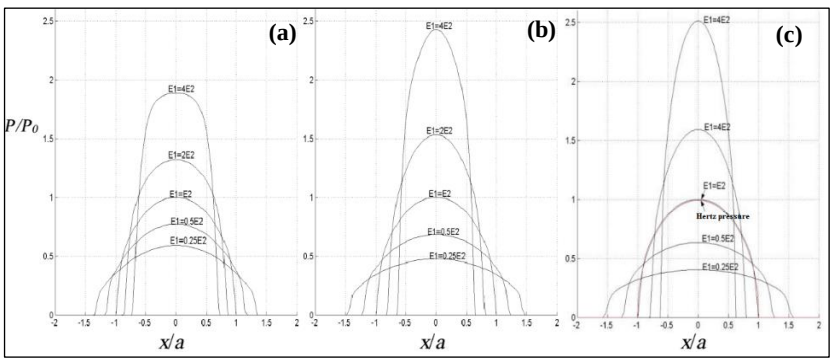

Figure 4: Profile of the pressure normalized by P_0, on x-axis for different values of E_1/E_2 and for various coating thickness, (a): $h = r/10 = 0.615a_0$, (b): $h = r/5 = 1.23a_0$, (c): $h = r = 6.15a_0$

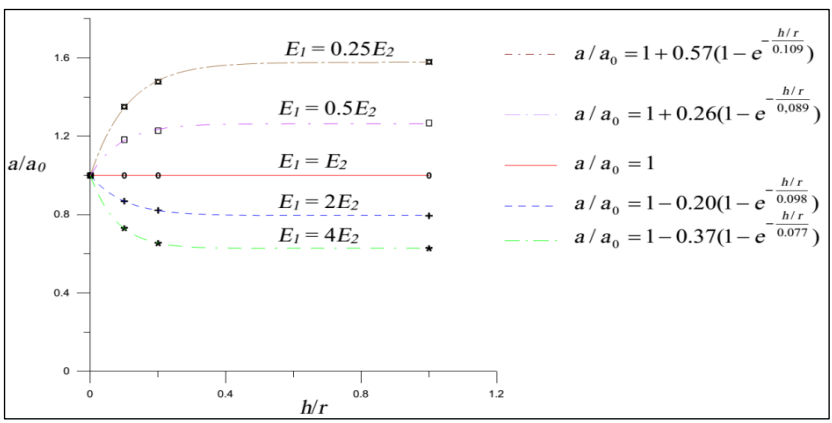

Figure 5: Contact radius a versus (h/r)

The calculation shows that the contact radius (a) obeys in all cases an exponential law given by the equation (25):

$$a / a_0 = 1 + b(1 - e^{-\frac{h/r}{c}}) \tag{25}$$

Table 1 presents the numerical values of coefficients b and c, obtained from comparing Equation (25) with each curve in Figure 5.

Table 1: Numerical values of coefficients b and c

E_1/E_2	b	c
4	-0.37	0.077
2	-0.20	0.098
1	0	-
0.5	0.26	0.089
0.25	0.57	0.109

For a coating thickness greater than $0.4r$, the ratio (a/a_0) tends to a limit value for the four types of coating. The dimensionless contact pressure P_0 as a function of the ratio (h/r) is shown in Figure 6 for the different ratios (E_1/E_2). It obeys an exponential law (Figure 6):

$$P / P_0 = 1 + b(1 - e^{-\frac{(h/r)^d}{c}}) \tag{26}$$

where b, c, and d are provided in Table 2. This table presents the numerical values of these coefficients, obtained from comparing Equation (26) with each curve in Figure 6 for the different ratios (E_1/E_2):

Table 2: Numerical values of coefficients b, c, and d

E_1/E_2	b	c	d
4	1.51	1.70	0.02
2	0.59	1.52	0.038
1	0	-	-
0.5	-0.36	1.079	0.087
0.25	-0.59	0.97	0.117

For (h/r) greater than 0.4, as for the contact zone (Figure 5), the maximal pressure tends towards the limit value corresponding to the solid without coating.

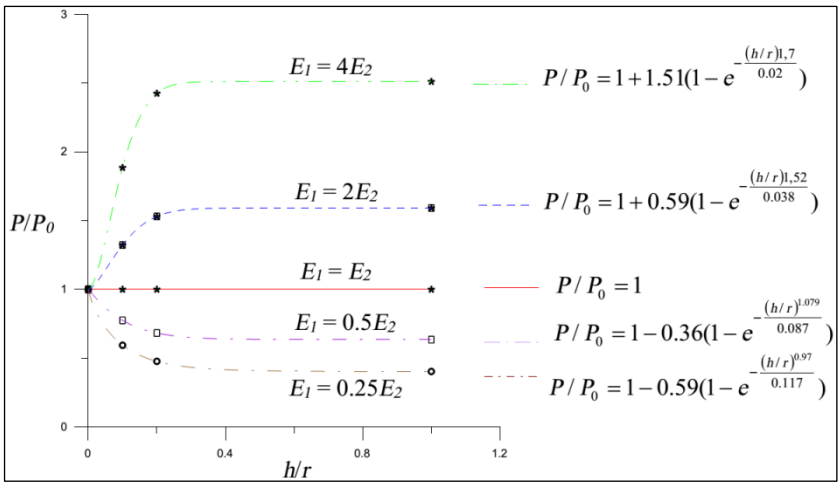

Figure 6: Maximal pressure according to *h/r*

Maximal principal stress and Von Mises stresses

About the coatings more rigid than the substrate and low thicknesses ($h = r/10$ and $h = r/5$), the maximal principal stress is on the *z*-axis at the level of the interface coating-substrate (Figure 7). This stress is generally much higher than that present on the surface on the *x*-axis. It is responsible for the fragile rupture type at the interface. However, its progression toward the surface is stopped by a strong compressive zone. On the other hand, for the rigid and thick coating ($h = r$), the high stress is always located on the surface and is negligible on the level of the interface coating-substrate.

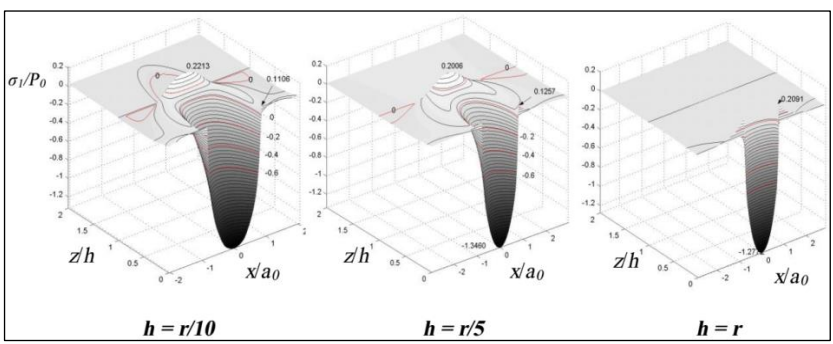

Figure 7: Maximal principal stress for a rigid coating ($E_1 = 2E_2$), for three coating thicknesses when friction coefficient $\mu = 0$

Let us note that for the case where $E_1 = E_2$, the maximal principal stress is always located on the surfaces in the contact zone, as in point $x = - a_0$ [21]. For the flexible coating ($E_1 = 0.25E_2$ and $E_1 = 0.5E_2$), the position of the maximal principal stress is always in the coating thickness.

Figure 8 presents the variation of the maximal principal stress on the surface along the x-axis, for various values of E_1/E_2 and various values of the coating thickness.

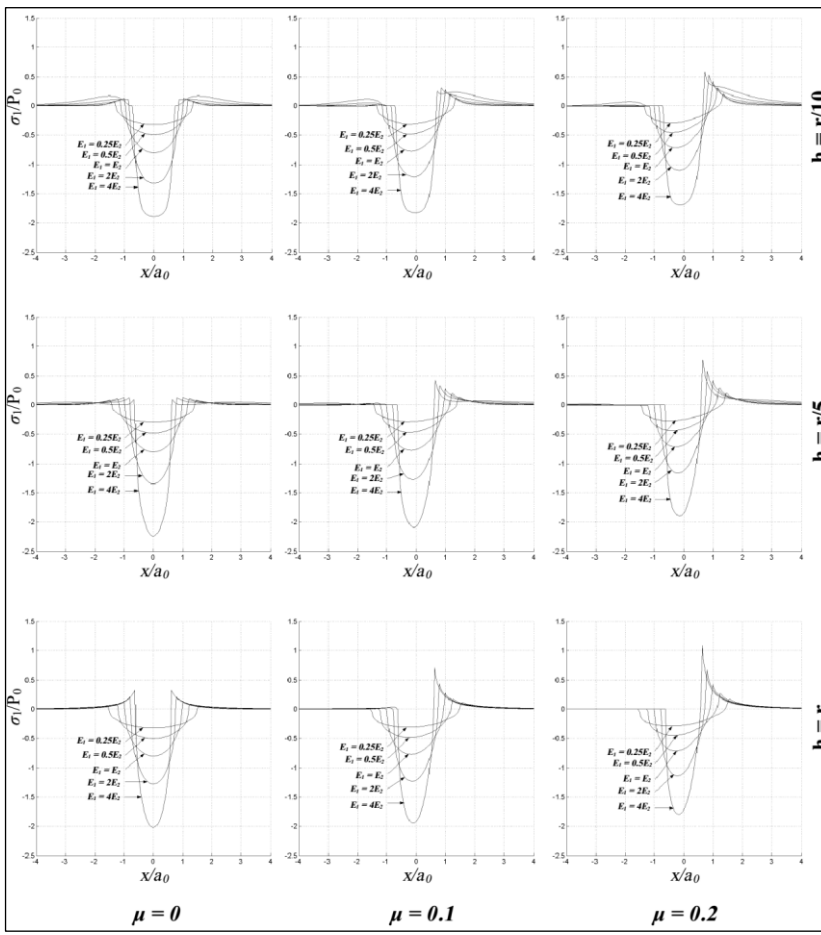

Figure 8: variation of the maximal principal stress on the surface, along the x-axis, for different values of E_1/E_2 and two coating thicknesses

For rigid coatings, the maximal traction stress for the three values of the coating thickness increases considerably if the friction coefficient increases too. For a null friction coefficient, in the case where $h = r/10$ and for the most rigid coating ($E_1 = 4E_2$), curiously, the maximum value of the tensile stress is not located on the zone of contact anymore but outwards as in points $x = 1.506a_0$ and $x = -1.506a_0$. This phenomenon is observed on the curves of variation of σ_{xx}/P_0 on the x-axis of O'sullivan [7], Hamilton [31], and Bhushan [32] where a local maximum appears in $x = -1.6a_0$ and $x = 1.6a_0$. However, it is a less perceptible bus in their modeling's, O'sullivan and Bhushan have chosen $E_2 = 100$ GPa and the most rigid coating was $E_1 = 2E_2$.

The Von Mises stress is defined by the following relation, where J_2 is the second invariant of tensor stress.

$$\sqrt{J_2} = \left(\sigma_{xy}^2 + \sigma_{xz}^2 + \sigma_{yz}^2 + \frac{1}{6}\left[(\sigma_{xx} - \sigma_{yy})^2 + (\sigma_{xx} - \sigma_{zz})^2 + (\sigma_{yy} - \sigma_{zz})^2 \right] \right)^{1/2} \quad (27)$$

Figure 9 represents the iso values of $\sqrt{J_2} / P_0$ for various values of coating thickness and various E_1/E_2 ratios. In the case of static contact, the isocontours of $\sqrt{J_2} / P_0$ have an axial symmetry. The maximum value of $\sqrt{J_2} / P_0$ is on the z-axis. The discontinuities appear at the level of the interface in the nonhomogeneous case ($E_1 \neq E_2$). It appears that in the case where the coating $h = r/10 = 0.615a_0$, the maximum value $\sqrt{J_2} / P_0$ increases by 190% when $E_1 = 4E_2$ and decreases by 42% when $E_1 = 0.25E_2$ compared to the case of not coated. Moreover, the position on the z-axis of the maximum $\sqrt{J_2} / P_0$ tends to go down towards the interface when the coating rigidity increases. It is located in $z = h$ starting from $E_1 = 2E_2$. The presence of a rigid coating increases the value of $\sqrt{J_2} / P_0$ in the substrate, and conversely, a flexible coating decreases this value.

With regards to the two other values of the coating thickness ($h = r/10 = 0.615a_0$ and $h = r = 6.15a_0$), the position of the maximum $\sqrt{J_2} / P_0$ goes up towards the surface when the ratio E_1/E_2 increases. The coating $h = r/10$ presents discontinuities at the level of the interface, whereas it is not the case for the coating $h = r$. For $h = r$, at the level of the interface coating-substrate, the value $\sqrt{J_2} / P_0$ is zero, this coating behaves like a solid body with E_1.

When the friction coefficient increases, the isovalues of $\sqrt{J_2} / P_0$ are not symmetrical anymore compared to the z-axis (Figure 10).

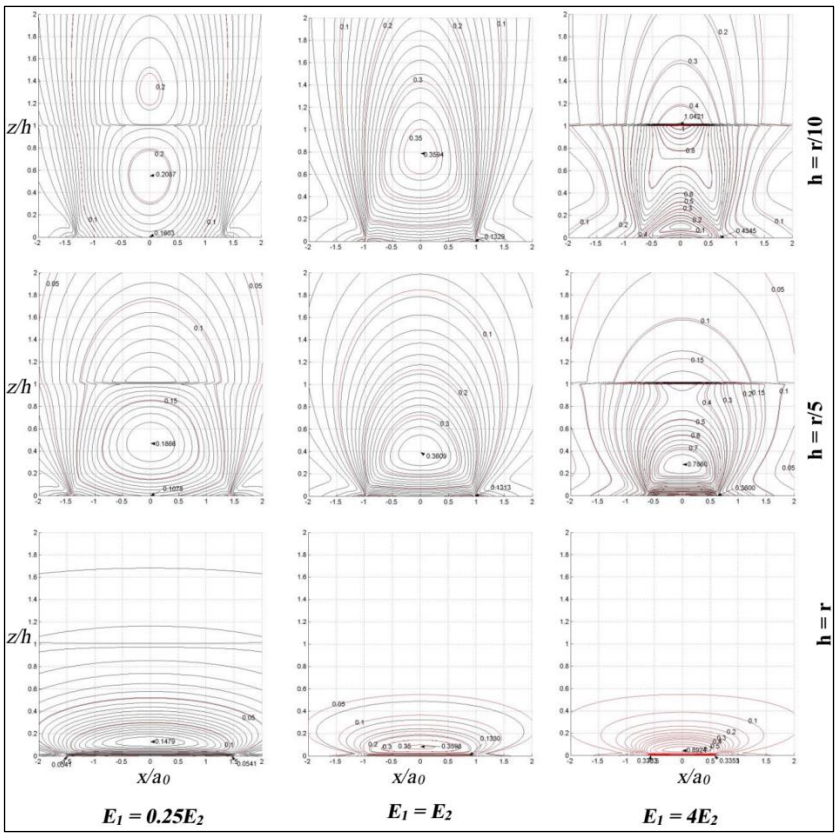

Figure 9: Isocontours of the normalized Von Mises stresses $J_2^{1/2} / P_0$ on the plan $y = 0$, for $E_1 = 0.25E2$, $E_1 = E_2$, and $E_1 = 4E_2$, and two coating thickness when $\mu = 0$ (static contact)

In Figure 10, the isovalues of $\sqrt{J_2} / P_0$ are reported for a friction coefficient value $\mu = 0.2$ on the same coatings. Let us note that for the finest and most rigid coating, the maximum value (at the level of the interface) of $\sqrt{J_2} / P_0$ increases only by 0.7% compared to the static case, whereas at the surface of the coating, it increases by 46%.

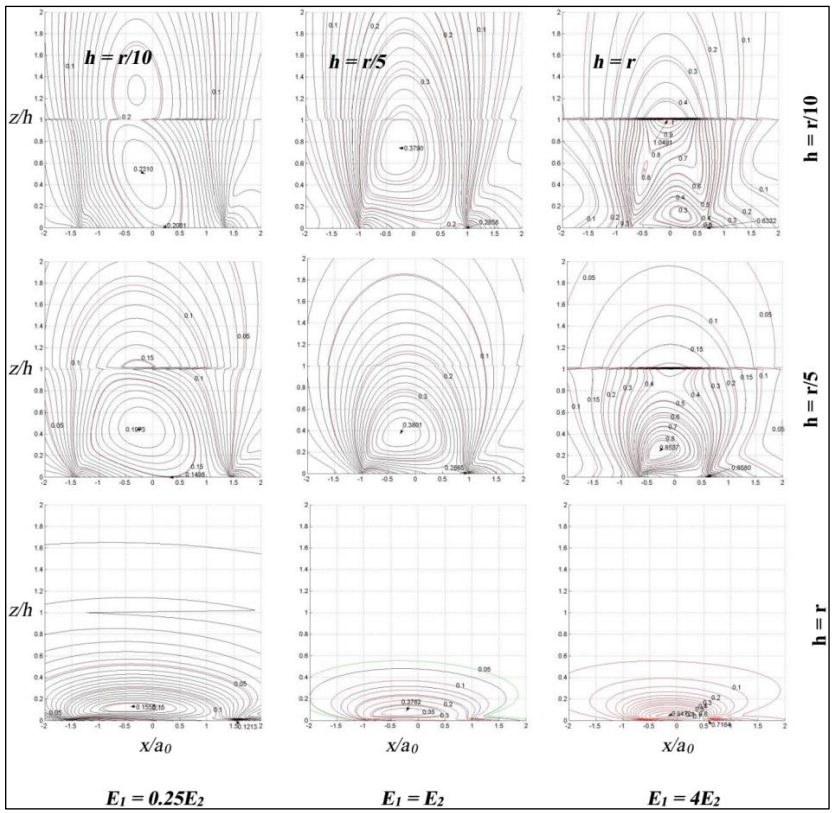

Figure 10. Isocontours of the normalized Von Mises stresses $J_2^{1/2} / P_0$ on the plan $y = 0$, for $E_1 = 0.25E2$, $E_1 = E_2$, and $E_1 = 4E_2$, for two coating thickness when $\mu = 0.2$ (dynamical sliding)

Rough contact: pressure, displacements, and contact area

Using the previously described model, a Rockwell indentation simulation (R = 0.2 mm) was performed on a rough DLC coating deposited on a steel substrate. The mechanical characteristics of the two materials are E_1 = 800 GPa, v_1 = 0.3, and E_2 = 200 GPa, v_2 = 0.3. During the simulation, a mesh of 101 x 101 points (10201 points) was used, with a pitch of mesh $\Delta x = \Delta y$ = 0.05 µm. The mesh is therefore performed on a total surface of 5 x 5 µm.

First, a rough surface with the same roughness parameters as the surface of the sample measured by AFM, where the mean line is the reference line and the mean roughness step is A_r = 0.33 µm, was digitally created. The rough surface is assumed to be isotropic, and the value of σ is 13.4 nm. Figure 11 shows the real profile and the simulated profile of the DLC sample.

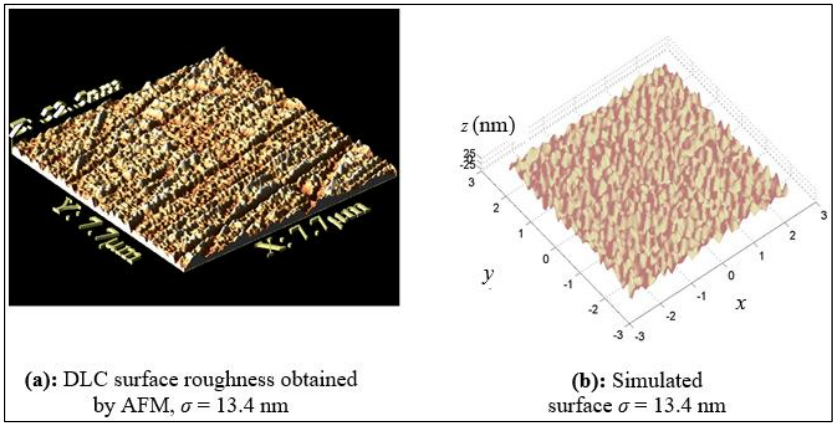

(a): DLC surface roughness obtained by AFM, $\sigma = 13.4$ nm

(b): Simulated surface $\sigma = 13.4$ nm

Figure 11: DLC surface roughness

A normal force density of 2 N/mm^2 was applied to this coating and then increased step by step to visualize the evolution of the contact pressure, and displacements along the *z*-axis depending on the load. The different simulations of contact pressures clearly show that, on one hand, new contact points appear when the normal force increases and, on the other hand, that the pressure peaks tend to increase.

The displacements of the contact surface appear at the levels of the contact asperities for low normal loads. When the normal load increases, the displacements of the asperities increase and add to the displacements of the whole surface $z = 0$. The superposition of the two displacements is then observed. Figure 12 gives the pressure fields as well as the corresponding displacements along the *z*-axis for an applied normal load $N = 10$ MPa on the same surface roughness, the same coating thickness $h = 20$ µm, but for different coating Young's modulus.

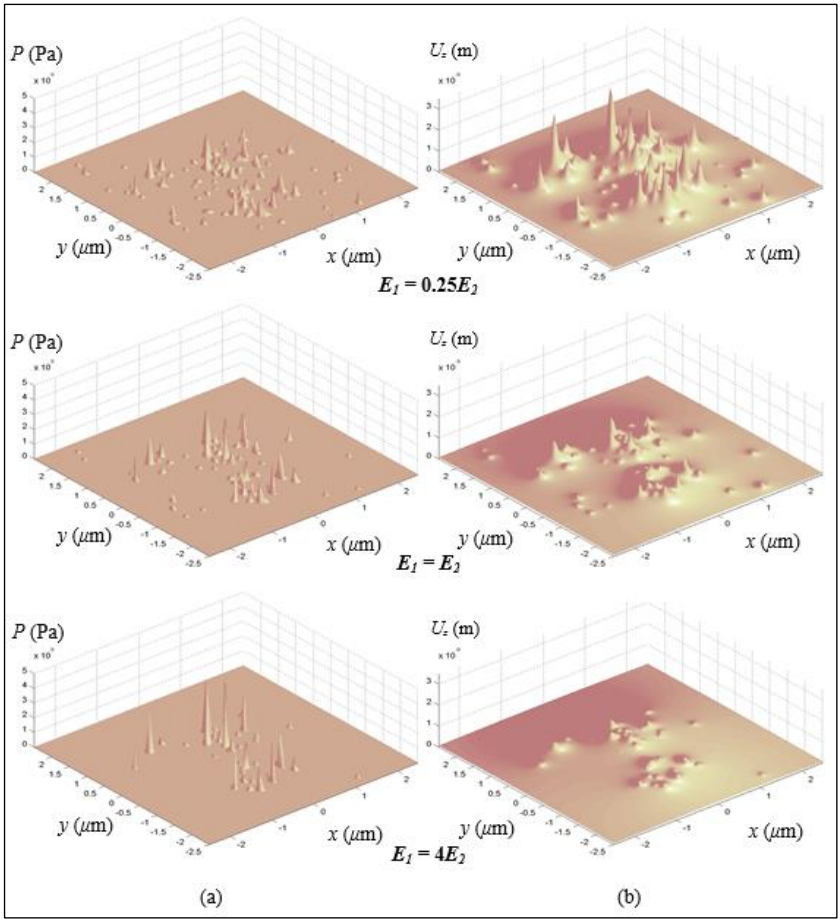

Figure 12: (a) evolution of the pressure field, (b) evolution of the displacement as a function of the ratio E_1/E_2 for a normal load N = 10 MPa and for the same coating thickness h = 20 µm

Conclusion

In this study, a numerical model for unilateral quasi-static contact between a rigid sphere and an elastic coating has been developed. The contact problem was solved by a numerical procedure based on the double Fourier transform and the Papkovich–Neuber potentials, for various coatings in different thicknesses and mechanical properties. The obtained results lead to the following conclusions:

a) For a rigid coating than the substrate, the contact pressure increases when the coating is increasingly thicker or more rigid. At the same time, the contact radius decreases when the coating is more and more rigid or when its thickness increases.
b) For a ductile coating that is more flexible than the substrate, the contact pressure decreases when the coating is increasingly thicker or more flexible. The contact radius increases when the coating becomes more flexible or its thickness increases.
c) In the case of the thinnest and most rigid coating, the maximal value of the surface stress is outside the contact zone for the low friction coefficients. A thick coating behaves like a solid body.
d) The various examples studied show clearly that the tribological behavior of a coated surface depends on the coating thickness and hardness and the friction coefficient value.

Contributions of Authors

The authors confirm the equal contribution in each part of this work. All authors reviewed and approved the final version of this work.

Funding

This work received no specific grant from any funding agency.

Conflict of Interests

All authors declare that they have no conflicts of interest.

Acknowledgment

We would like to extend our gratitude to all those who contributed to the success of this research project. Additionally, we appreciate the constructive comments and suggestions from the anonymous reviewers, which helped us to improve the manuscript.

References

[1] H. Hertz, "On The Contact Of Rigid Elastic Solids and On Hardness," in Miscellaneous Papers, Macmillan: London, UK, Chapter VI, pp. 163–183, 1896.

[2] E. Antaluca, "Contribution à l'étude des contacts," Thèse INSA de Lyon, 2005.

[3] T.F. Conry, A. Seireg, "A mathematical programming method for design of elastic bodies in contact," *Journal of Applied Mechanics*, vol. 38, no. 2, pp. 387-392, 1971.

[4] Y. P. Chiu, M. J. Hartnett, "A numerical solution for layered solid contact problems with application to bearings," *Journal of Lubrication Technology*, vol. 105, no. 4, pp. 585-590, 1983.

[5] T. Nogi, T. Kato, "Influence of a hard surface layer on the limit of elastic contact - Part I: Analysis using a real surface model", *Journal of Tribology*, vol. 119, no. 3, pp. 493-500, 1997.

[6] J. J. Kalker, W. Ingenieur, and G. T. Gravenhage, "On the rolling contact of two elastic bodies in the presence of dry friction," *Wear*, vol. 11, no. 4, pp. 303, 1968.

[7] T. C. O'Sullivan, R. B. King, "Sliding contact stress field due to a spherical indenter on a layered elastic half-space," *Journal of Tribology*, vol. 110, no. 2, pp. 235-240, 1988.

[8] W. Peng, B. Bhushan, "A numerical model for the contact of layered solids with rough surfaces by variational principle," *Journal of Tribology*, vol. 123, no. 2, pp. 330-342, 2001.

[9] F. I. Stepanov, E. V. Torskaya, "Modeling of sliding of a smooth indenter over a viscoelastic layer coupled with a rigid base," *Mechanics of Solids*, vol. 53, no. 1, 60-67, 2018.

[10] S.Plumet, M. C. Dubourg, "A 3-D model for a multilayered body loaded normally and tangentially against a rigid body: Application to specific coatings," *Journal of Tribology*, vol. 120, no. 4, pp. 668-676, 1998.

[11] Z. J. Wang, W. Z. Wang, H. Wang, D. Zhu, and Y. Z. Hu, "Partial slip contact analysis on three-dimensional elastic layered half space," *Journal of Tribology,* vol. 132, no. 2, pp. 1-12, 2010.

[12] Y. Xi, M. Björling, & A. Almqvist, "A numerical model for solving three-dimensional rolling contact problems with elastic coating layers," *Tribology Letters*, vol. 69, no. 139, pp. 2021.

[13] Z. Wang, X. Jin, L. M. Keer, Q. Wang, "A numerical approach for analyzing three-dimensional steady-state rolling contact including creep using a fastsemi-analytical method," *Tribology Transactions*, vol. 55, no. 4, pp. 446–457, 2012.

[14] E. Y. Manyo, P. Reynaud, B. Picoux, R. Tautou, F. Allou, C. Petit, D. Nelias, "Tire–pavement tractive rolling contact under turning conditions:

towards pavement top-down cracking," *International Journal of Pavement Engineering*, vol. 23, no. 3, pp. 1–10, 2020.

[15] J. Xu, K. Wang, X. Liang, Y. Gao, Z. Liu, R. Chen, P. Wang, F. Xu, K. Wei, "Influence of viscoelastic mechanical properties of rail pads on wheel and corrugated rail rolling contact at high speeds," *Tribology International*, vol. 151, pp. 1-15, 2020.

[16] X. Zhang, Q. J. Wang, T. He, "Transient and steady-state viscoelastic contact responses of layer-substrate systems with interfacial imperfections," *Journal of The Mechanics and Physics of Solids*, vol. 145, pp. 1-25, 2020.

[17] V.T. Nguyen, C. Hwu, "Time-stepping method for frictional contact of anisotropic viscoelastic solids," *International Journal of Mechanical Science*, vol. 184, pp. 1-15, 2020.

[18] E. R. Wallace, T. Chaise, D. Nelias, "Three-dimensional rolling/sliding contact on a viscoelastic layered half-space," *Journal of The Mechanics and Physics of Solids*, vol. 143, pp. 1-26, 2020.

[19] N. Menga, G. Carbone, D. Dini, "Exploring the effect of geometric coupling on friction and energy dissipation in rough contacts of elastic and viscoelastic coatings," *Journal of The Mechanics and Physics Solids*, 148, 104273, 2021.

[20] E. R. Wallace, T. Chaise, D. Nelias, "Rolling contact on a viscoelastic multi-layered half-space," *International Journal of Solids and Structures*, vol. 239-240, no. 6, pp. 111388, 2022.

[21] A. Bettayeb, B. Villechaise, "Analyse des contraintes et des déformations d'un secteur circulaire revêtu. Approche analytique nouvelle," 11ème congrès CFM Lille, 1993.

[22] P. K. Gupta, J. A. Walowit and E. F. Finkin, "Stress distributions in plan strain layered elastic solids," *Journal of Lubricant and Technology*, vol. 96, no. 4, pp. 427-432, 1973.

[23] P. Fu, J. Zhao, X. Zhang, H. Miao, Z. Wen, G. Kang, Q. Kan, "Three-dimensional tractive rolling contact analysis of functionally graded coating-substrate systems with interfacial imperfection and frictional anisotropy," *Composite Structures*, vol. 307, p. 116671, 2023.

[24] X. W. Chen, Z. Q. Yue, "Incomplete contact between a coated elastic substrate and rigid foundation perturbed by a rigid disc," *International Journal of Solids and Structures*, vol. 202, pp. 605–19, 2020.

[25] X. Zhang, Q. J. Wang, Y. Wang, Z. Wang, H. Shen, J. Liu, "Contact involving a functionally graded elastic thin film and considering surface effects," *International Journal of Solids and Structures*, vol. 150, pp. 184–96, 2018.

[26] T. S. Vasu, T.K. Bhandakkar, "Plane strain cylindrical indentation of functionally graded half-plane with exponentially varying shear modulus in the presence of residual surface tension," *International Journal of Mechanical Sciences*, vol. 135, pp. 158–67, 2018.

[27] H. Zhang, W. Wang, S. Zhang, Z. Zhao, "Semi-analytical solution of three-dimensional steady state thermoelastic contact problem of multilayered material under friction heating," *International Journal of Thermal Sciences*, vol. 127, pp. 384–99, 2018.
[28] T. Wang, X. Ma, L. Wang, L. Gu, L. Yin, J. Zhang, L. Zhan, and D. Sun, "Three-dimensional thermoelastic contact model of coated solids with frictional heat partition considered," *Coatings*, vol. 8, no. 12, pp. 1-20, 2018.
[29] Y. Zhou, C. Zhang, Z. Zhong, L, Wang, "Transient thermo-electro-elastic contact analysis of a sliding punch acting on a functionally graded piezoelectric strip under non-Fourier heat conduction," *European Journal of Mechanics - A/Solids*, vol. 73, pp. 90–100, 2019.
[30] L.Malvern, Introduction Of Mechanics Of A Continuous Medium, Prentice-Hall, 1969.
[31] G. M. Hamilton and L. E. Goodman, "The stress field created by a circular sliding contact," *Journal of Applied Mechanics*, vol. 33, no. 2, pp. 371-376, 1966.
[32] Bhushan, B., "Contact mechanics of rough surfaces in tribology: Multiple asperity contact", *Tribology Letters*, vol. 4, pp. 1-35, 1998.

Appendix 1

By introducing a double FFT on the relations (3) and (4) containing terms in *x*, the three unknown factors $B^{(1)}, \bar{B}^{(1)}$ et $B^{(2)}$ are solved in the frequency domain by:

$$\bar{B}^{(1)} = \left\{ \frac{(G-1)e^{-2\alpha h}}{(1+G)+(1-G)e^{-2\alpha h}} \right\} \frac{\mu \bar{P}(\xi,\eta,0)}{2\alpha(1-\nu_1)}$$

$$B^{(1)} = \bar{B}^{(1)} + \frac{\mu \bar{P}(\xi,\eta,0)}{2\alpha(1-\nu_1)}$$

$$B^{(2)} = \left\{ \frac{e^{-\alpha h}}{(1+G)+(1-G)e^{-2\alpha h}} \right\} \frac{\mu \bar{P}(\xi,\eta,0)}{2\alpha(1-\nu_1)} \frac{2(1-\nu_1)}{(1-\nu_2)}$$

The system of nine equations to nine unknown factors $A^{(1)}, \bar{A}^{(1)}, B^{(1)}, \bar{B}^{(1)}, C^{(1)}, \bar{C}^{(1)}, A^{(2)}, B^{(2)}, C^{(2)}$ is simplified with a system of six equations to six unknown factors:

$$
\begin{aligned}
&\alpha A^{(1)} - \alpha \bar{A}^{(1)} + (1-2\nu_1)C^{(1)} + (1-2\nu_1)\bar{C}^{(1)} = \alpha R_1 \\
&\alpha A^{(1)} - \alpha \bar{A}^{(1)} + 2(1-2\nu_1)C^{(1)} - 2(1-\nu_1)\bar{C}^{(1)} = \alpha R_2 \\
&\alpha A^{(1)} - \alpha e^{2\alpha h}\bar{A}^{(1)} + \{(1-2\nu_1)+\alpha h\}C^{(1)} + \{(1-2\nu_1)-\alpha h\}e^{2\alpha h}\bar{C}^{(1)} \\
&-\alpha e^{\alpha h}A^{(2)} - (1-2\nu_2)e^{\alpha h}C^{(2)} = \alpha R_3 \\
&\alpha A^{(1)} + \alpha e^{2\alpha h}\bar{A}^{(1)} + \{2(1-\nu_1)+\alpha h\}C^{(1)} - \{2(1-\nu_1)-\alpha h\}e^{2\alpha h}\bar{C}^{(1)} \\
&-\alpha e^{\alpha h}A^{(2)} - 2(1-\nu_2)e^{\alpha h}C^{(2)} = \alpha R_4 \\
&\alpha A^{(1)} + \alpha e^{2\alpha h}\bar{A}^{(1)} + \alpha hC^{(1)} + \alpha he^{2\alpha h}\bar{C}^{(1)} - G\alpha e^{\alpha h}A^{(2)} = \alpha R_5 \\
&\alpha A^{(1)} - \alpha e^{2\alpha h}\bar{A}^{(1)} + \{(3-4\nu_1)+\alpha h\}C^{(1)} + \{(3-4\nu_1)-\alpha h\}e^{2\alpha h}\bar{C}^{(1)} \\
&-G\alpha e^{\alpha h}A^{(2)} - G(3-4\nu_2)e^{\alpha h}C^{(2)} = \alpha R_6
\end{aligned}
$$

whose

Solution in the frequential field is:

$$
\begin{aligned}
C^{(1)} &= \frac{(1-\lambda)kS_0R_c}{4(1-\nu_1)(G-1)\left\{1-(\lambda+k+4k\alpha^2h^2)e^{-2\alpha h}+\lambda ke^{-4\alpha h}\right\}} \\
\bar{C}^{(1)} &= \frac{2(G-1)\alpha he^{-2\alpha h}C^{(1)} + e^{-2\alpha h}R_a}{S_0} \\
A^{(1)} &= \frac{(-3+4\nu_1)C^{(1)} + \bar{C}^{(1)} + \alpha(R_1+R_2)}{2\alpha} \\
\bar{A}^{(1)} &= \frac{(1-\lambda)e^{-2\alpha h}C^{(1)} + ((3-4\nu_1)(1-e^{-2\alpha h}) - 2\alpha h)\bar{C}^{(1)} + e^{-2\alpha h}R_d}{2\alpha(1-e^{-2\alpha h})} \\
C^{(2)} &= \frac{4(1-\nu_1)(1-\lambda)e^{-\alpha h}C^{(1)} + (1-\lambda)\alpha e^{-\alpha h}(R_3-R_4+R_5-R_6)}{4(1-\nu_1)} \\
A^{(2)} &= \frac{2\alpha he^{-\alpha h}(S_0-(G-1)(1-e^{-2\alpha h}))C^{(1)} - (3-4\nu_2)S_0C^{(2)}}{2\alpha S_0} \\
&+ \frac{\alpha e^{-\alpha h}S_0(R_1+R_2-R_3-R_4) - (1-e^{-2\alpha h})e^{-\alpha h}R_a}{2\alpha S_0}
\end{aligned}
$$

where $R_1, R_2, R_3, R_4, R_5,$ and R_6 are:

$$R_1 = -\frac{1}{\alpha^2}\left(i\,\xi(B^{(1)} - \bar{B}^{(1)}) + i\,\alpha^2(B_{,\xi}^{(1)} - \bar{B}_{,\xi}^{(1)})\right)$$

$$R_2 = -\frac{1}{\alpha^2}\left(2i\,\xi(1-\nu_1)(B^{(1)} + \bar{B}^{(1)}) + i\,\alpha^2(B_{,\xi}^{(1)} + \bar{B}_{,\xi}^{(1)}) + \bar{P}(\xi,\eta)\right)$$

$$R_3 = -\frac{1}{\alpha^2}(i\,\xi(1-\alpha h)B^{(1)} - i\,\xi(1+\alpha h)e^{2\alpha h}\bar{B}^{(1)} - i\,\xi e^{\alpha h}B^{(2)}$$
$$+i\,\alpha^2(B_{,\xi}^{(1)} - e^{2\alpha h}\bar{B}_{,\xi}^{(1)}) - i\,\alpha^2 e^{\alpha h}B_{,\xi}^{(2)})$$

$$R_4 = -\frac{1}{\alpha^2}((2i\,\xi(1-\nu_1) - i\,\xi\alpha h)B^{(1)} + (2i\,\xi(1-\nu_1)$$
$$+i\,\xi\alpha h)e^{2\alpha h}\bar{B}^{(1)} - 2i\,\xi(1-\nu_2)e^{\alpha h}B^{(2)})$$
$$-\frac{1}{\alpha^2}\left(i\,\alpha^2 B_{,\xi}^{(1)} + i\,\alpha^2 e^{2\alpha h}\bar{B}_{,\xi}^{(1)} - i\,\alpha^2 e^{\alpha h}B_{,\xi}^{(2)}\right)$$

$$R_5 = -\frac{1}{\alpha^2}(-i\,\xi\alpha h B^{(1)} + i\,\xi\alpha h e^{2\alpha h}\bar{B}^{(1)} + i\,\alpha^2 B_{,\xi}^{(1)}$$
$$+i\,\alpha^2 e^{2\alpha h}\bar{B}_{,\xi}^{(1)} - i\,\alpha^2 G e^{\alpha h}B_{,\xi}^{(2)})$$

$$R_6 = -\frac{1}{\alpha^2}(i\,\xi(1-\alpha h)B^{(1)} - i\,\xi(1+\alpha h)e^{2\alpha h}\bar{B}^{(1)} - i\,\xi G e^{\alpha h}B^{(2)}$$
$$+i\,\alpha^2(B_{,\xi}^{(1)} - e^{2\alpha h}\bar{B}_{,\xi}^{(1)}) - i\,\alpha^2 G e^{\alpha h}B_{,\xi}^{(2)})$$

and, R_a, R_b and R_c are:

$$R_a = (G-1)\alpha(R_1 + R_2) - G\alpha(R_3 + R_4) + \alpha(R_5 + R_6)$$
$$R_b = \alpha(R_2 - R_1) + \alpha e^{-2\alpha h}(R_3 - R_4)$$
$$R_c = \left(\frac{2\alpha h e^{-2\alpha h}}{S_0}R_a + R_b\right)\frac{4(1-\nu_1)}{1-\lambda}$$
$$R_d = \alpha(R_1 - R_2 - R_3 + R_4) + (R_3 - R_4 + R_5 - R_6)\frac{\alpha(1-\lambda)}{4(1-\nu_1)}$$

Appendix 2

Part of the program code (in MATLAB) used in this paper:

```
%-------------------------------------------------
% calcul de la pression cas mutlitcouche
%-------------------------------------------------

clear all
time0=clock;
```

```
[time0(4) time0(5) time0(6)]

varianc=2;%en c'est la rugosité nm avant c'etait
13.4

coefbloc1=revetavec2_matrice;
pip=size(coefbloc1)
load paraminit.mat

rayon=R;
epsilon=0.1;delta_pen=R/8;
force=27.75;forcetest=8*force;

%--------------------------------------------------
%--------------------------------------------------

 j=0;
while(abs(force-forcetest)>epsilon)
j=j+1;
jemeboucledewhile=j
Uzm=[];kk=[];
m=n^2;
for k=1:m
.
.
.
rugo=Rug';
rugos=[];
s=size(rugo,1); r=sqrt(s);
for j=1:r
   rugos=[rugos;rugo(1+(j-1)*r:j*r)'];
end

P1=[];
s=size(p1,1); r=sqrt(s);
for j=1:r
   P1=[P1;p1(1+(j-1)*r:j*r)'];
end

figure(25)
plot(nombrenegatifs,'r.')
hold on
plot(nombrenegatifs)
```

```
 for k=1:m
    Rugi(k)=(10^-9)*varianc*randn(1,1);
end
pip=Rugi';
rugosite=[];
s=size(pip,1); r=sqrt(s);
for j=1:r
   rugosite=[rugosite;pip(1+(j-1)*r:j*r)'];
end


 figure(30)
surfl(x,y,rugosite);
 shading interp;
 colormap(pink);

 time=clock;
heure=time(4)-time0(4)
```